Heterogeneous nucleation of colloidal melts under the influence of shearing fields

2004 J. Phys.: Condens. Matter 16 S3885

(http://iopscience.iop.org/0953-8984/16/38/008)

INSTITUTE OF PHYSICS PUBLISHING JOURNAL OF PHYSICS: CONDENSED MATTER

J. Phys.: Condens. Matter **16** (2004) S3885–S3902 PII: S0953-8984(04)78987-0

Heterogeneous nucleation of colloidal melts under the influence of shearing fields

Andreas Stipp[1], Ralf Biehl[2], Thorsten Preis[1], Jianing Liu[1], Ana Barreira Fontecha[1], Hans Joachim Schöpe[1] and Thomas Palberg[1]

[1] Institute of Physics, University of Mainz, Germany
[2] Institute for Solid State Research, Forschungszentrum Jülich, Germany

E-mail: Thomas.Palberg@uni-mainz.de

Received 13 April 2004, in final form 2 August 2004
Published 10 September 2004
Online at stacks.iop.org/JPhysCM/16/S3885
doi:10.1088/0953-8984/16/38/008

Abstract

Large, oriented single crystals may be obtained from shear melts of colloidal particles after nucleation at the container walls. We are here interested in the processes occurring during the initial phase of their formation. Using different microscopic and scattering techniques we here studied highly charged suspensions of spherical particles, dispersed in low salt or deionized water, in single and double wall confinement, during and after cessation of shear. While the equilibrium phase of our colloidal solids is body centred cubic, the shear induced precursors of heterogeneous nuclei consist of wall based, oriented, registered or freely sliding layers with in plane hexagonal symmetry. Cessation of shear initiates a complex heterogeneous nucleation process. If the layer structures are space filling, they register to form a meta-stable randomly stacked close packed hexagonal crystal. In double wall confinement the transformation to the equilibrium body centred cubic structure occurs on long timescales via nucleation and subsequent lateral growth. For non-space filling, wall based layer structures we find indications of competition between the decay of the layers in favour of the shear melt and their stabilization through registering and subsequent coverage by an epitaxially growing wall crystal. From quantitative growth curve measurements we obtain the initial wall crystal thickness d_0, which may serve as a lower bound to the extension of the layer structures under shear. We observe a pronounced dependence of d_0 on both former shear conditions and meta-stability of the melt.

(Some figures in this article are in colour only in the electronic version)

1. Introduction

From two sides there is a strong and increasing interest in the growth of single crystals of defined structure and orientation from colloidal shear melts. First, there are fascinating possible applications of such nano-structured materials as optical elements ranging from filters and diffraction grids to photonic band gap materials [1, 2]. Second, however, there is a large interest in nucleation and growth processes also from the fundamental point of view. Synthetic colloidal spheres have already been known to show crystallization for some time [3]. Their phase behaviour and their crystallization kinetics have attracted broad attention as test cases for statistical mechanical modelling of equilibrium properties [4–6] and as a model case for dynamic processes of nucleation and growth [7–11]. This was triggered by their excellent optical accessibility by time resolved complementary methods from real and reciprocal space, and by the convenient colloidal timescales of milliseconds to hours. Another advantage is the possibility to experimentally adjust the nature and the strength of the particle interaction over a wide range between the theoretical limits of hard spheres and the one component plasma for purely repulsive systems or to add attractive terms of entropic or dipolar nature. Moreover, in most cases the interaction can be represented in a compact form as an effective pair energy of, e.g. Yukawa type, facilitating efficient computer simulations [4, 7].

Recently, for systems solidifying under mechanically undisturbed bulk situations the classical theories of nucleation and growth could be generally confirmed. Nucleation follows a classical activated route [8, 12–14], growth is reaction controlled in charged systems and diffusion controlled in hard sphere systems, with inter-related kinetic pre-factors [9]. Even more interesting are the subtle deviations also observed, like non-spherical shapes of nuclei [15], the influence of polydispersity [16], the effect of mixing different species [17, 18], growth instabilities [19–21], and the scenarios observed in competition with the kinetic glass transition [22, 23]. Most exciting, however, is the effect of additional external fields to control both nucleation and growth processes. Here a wide variety of technical realizations has been applied to optimize crystal quality and study specific effects. These range from the influence of gradients of temperature or chemical potential [24, 25], over gravity [26, 24, 27], electric fields [28–30] and pre-structured substrates [31, 27, 32, 33] to shearing fields [34–38]. In most cases the influence of walls turned out to be crucial in controlling heterogeneous nucleation and subsequent growth. As revealed by experiment, theory and simulation, both equilibrium phase behaviour [2, 39–42] and solidification kinetics [34, 38, 43] in the presence of confining walls differ considerably from bulk situations. Shear on the other hand, turned out to be a most versatile means to extend nucleation control at flat unstructured walls through the possibility of forming meta-stable shear-induced structures under flow. These may in principle determine the structure of the nuclei and thus the later morphology and orientation of the final crystal [44, 36, 37, 45–48]. The (surely still incomplete) compilation of references indicates the extraordinary efforts taken to gain a refined understanding and an improved control of the solidification process from colloidal melts. It further shows that we are beginning to obtain this understanding by an intense collaboration between experimental, theoretical and simulation approaches [49]. Key questions now concern the mechanisms by which shear induced structures relax into the final crystal state. These may range from complete decay into an isotropic shear melt and successive formation of heterogeneous nuclei at the container wall as one extreme to the, possibly martensitic, transformation of shear induced crystal-like structures directly into equilibrium crystals as the other. Previous investigations already indicated that the kinetic route taken by a specific system strongly depends on the experimental boundary conditions [50, 51].

Table 1. Compilation of particle data. All samples are of polystyrene stabilized by sulfate or carboxylate surface groups. The table shows the nominal diameter $2a$, measured particle radii a from dynamic light scattering (DLS) and static light scattering (SLS). The freezing and melting densities n_F and n_M refer to deionized conditions. They form the lower, respectively, upper boundary of the coexistence region. Also shown are the effective charges inferred from conductivity and elasticity measurements, Z^*_σ and Z^*_G, respectively.

No.	Batch No.	$2a_{NOM}$ (nm)	$2a$ (nm)	n_F (μm^{-3})	n_M (μm^{-3})	Z^*_σ	Z^*_G
PS120	IDC 10-202-66	120	128 (DLS) 121 (SLS)	0.34 ± 0.02	0.47 ± 0.05	685 ± 10	474 ± 10
PS156	IDC 2-179-4	156	—	0.07 ± 0.02	0.12 ± 0.02	945 ± 70	615 ± 50
PS301	IDC 10-66-58	301	322 ± 2.4 (DLS) 310 ± 4 (SLS)	0.05 ± 0.01	0.06 ± 0.01	2240 ± 60	—

In this contribution we present an experimental study on the *combined* influence of shear, confinement and interaction strength. We study colloidal shear melts of highly charged suspensions of spherical particles dispersed in low salt or deionized water in the presence of one or two flat walls during and after cessation of linear shear. Our aim is first to give an overview of the complex interplay of these two external fields and the resulting phenomenology. Second, we seek a *quantitative* estimate of the thickness of shear residues acting as a precursor for heterogeneous nucleation. This is performed by measurements of the initial wall crystal thickness d_0 and its dependence on interaction and shear parameters. Finally a more qualitative description of the transition from the meta-stable intermediate rhcp state to the final bcc structure for both cases of confinement is given. The paper is organized as follows. We start with a short introduction of samples and their conditioning. The observation techniques are presented in some detail, followed by the results for double wall confinement and single wall confinement. We shall close with a short discussion of the observed solidification scenarios.

2. Experimental details

2.1. Samples and sample conditioning

Three commercial, highly charged, low polydispersity samples were employed in our study. Samples were carefully characterized by various methods before use. Each was particularly suited in terms of size for the intended optical method. Table 1 compiles important data on the samples used. For the experiments in the plate–plate shear cell we used PS301. This large species is readily visible in the high resolution microscope. It has a low lying freezing transition at particle distances of about 1.5 μm enabling unequivocal particle discrimination. On the other side its scattering cross section is already too large to study bulk crystallization without multiple scattering effects. For the investigations in flow through cells we therefore employed two samples of lesser diameter.

Data on the principle verification of the registered to free sliding transition in the bulk were gathered on PS120. This species shows a body centred to face centred cubic transition (bcc to fcc) in equilibrium, located at particle number densities $2.7\ \mu^{-3} \leqslant n \leqslant 4.8\ \mu^{-3}$ [52]. Under shear at $n = 3\ \mu$m^{-3} it shows a space filling hexagonal layer structure. Data shown are first results of a larger enterprise still in progress, which studies the influence of this transition on the shear motion [53].

For the actual study on the heterogeneous nucleation of bcc crystals from hexagonal sliding layers, PS120 and PS156 and mixtures thereof were chosen at n close to the fluid–

solid coexistence. They show the formation of a bcc structure of random composition over the complete range of mixing number ratios $p_{156} = n_{156}/n$ (where n_{156} denotes the particle number density of PS156). Under shear they form wall based layer structures coexisting with a central shear melt.

As described in detail elsewhere, we conditioned our samples in a closed Teflon® tubing system under inert gas atmosphere [54–57]. The tubing connects different components. These comprise a mixed bed ion exchange column (filled with Amberlite UP 604, Rohm & Haas, Chancy, France), a reservoir under Ar atmosphere to add water, CO_2 or salt solution, a static light scattering cell to determine the particle number density n from the position of Bragg reflections, the actual microscopy cell and a conductivity experiment to control n for deionized suspensions or the salt concentration c for salty suspensions with known n. Usually, experiments at elevated salt concentration are performed using NaCl. In the experiments on PS301, c was altered by controlled contamination with air-borne CO_2. To this end the ion exchange column was by-passed after reaching a constant minimum conductivity σ_{MIN} indicating complete deionization. A known amount of air was then placed in the reservoir with a syringe. During this, pumping was continued and thus the contamination could be controlled *in situ* via conductivity increase: $c = (\sigma - \sigma_{MIN})/\Lambda_{H_2CO_3}$. Here $\Lambda_{H_2CO_3} = 39.415 \times 10^{-4}$ (S l) (cm mol)$^{-1}$ ($T = 298.15$ K) denotes the limiting molar conductivity at infinite dilution [58]. An overdose of CO_2 may be conveniently reduced by again pumping through the ion exchange column. This procedure turned out to be more accurate than the addition of nominally μ molar NaCl solutions, which always contained ill defined CO_2 and thus carbonate concentrations [59].

Effective charges were determined from conductivity measurements under deionized conditions and known n using: $\sigma_{MIN} = neZ^*(\mu_+ + \mu_-) + \sigma_B$, with $\sigma_B \approx 0.055$ nS cm^{-1} as the background conductivity of deionized water under room temperature and the proton mobility of $\mu_+ = 36.5 \times 10^{-8}$ m^2 V^{-1} s^{-1}. The mobility of particles μ_- was measured by laser Doppler electrophoresis to be in the range $\mu_- = (2\text{–}10) \times 10^{-8}$ m^2 V^{-1} s^{-1} [60]. Where particle mobilities were not known we used an estimate of $\mu_- = 5 \times 10^{-8}$ m^2 V^{-1} s^{-1} to obtain the values of Z^*_σ. For the smaller particles effective charges Z^*_G were also determined from measurements of the shear modulus G [61]. As seen in table 1, Z^*_G are slightly lower, but of the same order of magnitude as Z^*_σ. Both effective charges are much smaller than titrated charge numbers N.

2.2. High resolution shear microscopy for double wall confinement

To study doubly restricted geometries we used a newly developed shear microscope with plate–plate geometry at a plate separation adjusted to 30 μm. For PS301 prepared at $n = 0.15\ \mu$m^{-3} this corresponds to some 15 layers of particles filling the gap. The instrument has recently been described in detail elsewhere [62]. We here only note that shear rates between 0.5 and 15 s^{-1} are conveniently realized. Observation uses a 63× long distance high resolution objective allowing for single particle tracking (PL Fluotar L 63×/0.7 corr PH2 ∞/0.1–1.3/C; working distance 1800 μm, Leitz, Germany). By suitable manipulation of the cover glass correction we were able to considerably extend the depth of sharpness and project regions of three to five layers into the image plane. Time resolved high resolution microscopy is possible with sufficiently spaced particles. At particle distances of 2 μm, each micrograph contains some 7000 particles, which is sufficient to study the system structure and motion. To this end we constructed position correlation diagrams (PCDs) giving the conditioned probability of finding a second particle in the projection, given the first is at the origin. Technically this is equal to the construction of a pair correlation function, but due to the nature of the projection it is

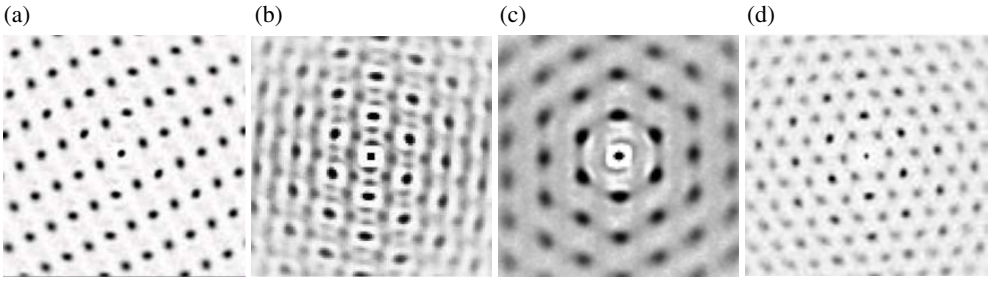

Figure 1. Example PCDs obtained from suspensions of PS301 at $n = 0.15\ \mu\text{m}^{-3}$ (a) bcc structure at rest, (b) under shear at $\dot{\gamma} = 0.35$ Hz, (c) under shear at $\dot{\gamma} = 7.9$ Hz and (d) after cessation of shear. Flow direction is upward. PCD width 13.1 μm. The central particle is contained in a 7×7 pixel area originating from image processing and containing no signal. Outside, a high probability of finding a particle image at a projected xy position is denoted by dark shading. Note that several layers are imaged simultaneously. This is best seen in (d), where the next layer positions are seen in mid grey in a hexagon of dark grey central layer positions. The hexagonal pattern is also present in (b) and (c). At the lower shear rate adjacent layer zig-zag traces and accumulation points corresponding to registered positions are visible. At the larger shear rate the adjacent layer particle probability is nearly isotropic. Only the in-plane hexagonal order remains clearly visible. ((a) and (d) reproduced from [63]. An overview of PCDs under different shear and interaction conditions can be found in [64]).

physically different and different information, e.g. the relative position of layers with respect to each other, may be obtained. In addition, from time averaged PCDs the relative motion can also be inferred with good statistics [62–64].

In the examples (partly reproduced from [63] and [64]) shown in figure 1 the depth of sharpness is of the order of five layers. Thus in figure 1(a) the projection of several (110) planes of the bcc structure at rest takes a rectangular appearance. Under shear it changes to a structure of randomly stacked hexagonal layers (rhcp). In figure 1(b) the zig-zag traces of adjacent layers of hexagonal structure and the accumulation points (positions of registering) are clearly visible under shear. Note from the orientation of the zig-zag-traces that the planes are oriented with their densest packed direction $\langle 111 \rangle$ parallel to the flow direction (upward). In figure 1(c) both traces and accumulation points have vanished and one observes a pronounced in-plane hexagonal structure on a near isotropic background probability of finding adjacent layer particles. Adjacent layer traces are only faintly visible and straight. The transition between figures 1(b) and (c) showing the registered zig-zag sliding and the unregistered straight sliding modes occurs with increased shear rate and was observed to be continuous.

In figure 1(d), taken immediately after the cessation of shear, the central layer is visible as a black hexagonal lattice, while the adjacent layers stacked in either AB or AC positions are visible in fainter grey. The shear induced orientation is retained upon registering. We further note that this cell-filling meta-stable structure is accessible from both registered and unregistered sliding layer structures, if the equilibrium phase in our slit geometry is bcc.

2.3. Light scattering analysis for single wall confinement

For the present work we employed optical flow through cells of rectangular cross section of macroscopic dimensions (2 mm $\times$ 10 mm or 1 mm $\times$ 10 mm, Rank Bros Ltd, Bottisham, Cambridge, UK). Independent velocity measurements as a function of cell depth using laser Doppler velocimetry show a parabolic flow profile [53]. Using the peristaltic pump to drive the flow, a periodic oscillation of the velocity was observed. Therefore two additional reservoirs were integrated into the tubing cycle between which the suspension flowed solely under the

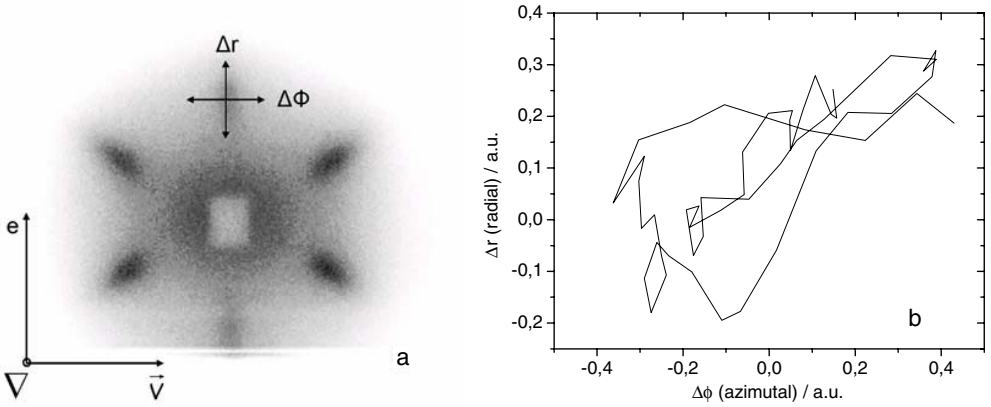

Figure 2. (a) Static light scattering pattern of a deionized sample of PS120 at $n = 3\ \mu\mathrm{m}^{-3}$ and a flux of 8 ml min^{-1}. High intensity is denoted by dark shading. The hexagonal scattering pattern is clearly visible. Note the somewhat reduced intensity of the upper $\{01\}$ reflection indicating the presence of a sliding layer structure (for a detailed discussion of scattering patterns see [36] and [66]). Also shown is the coordinate system used for monitoring motion of the reflection in reciprocal space: Δr radial direction; $\Delta\varphi$ azimuthal direction. Further we show the real space coordinates of the flow: v flow direction; Δ gradient direction; e vorticity direction. (b) Time trace of the upper $\{10\}$ reflection in the Δr–$\Delta\varphi$-plane over a period of 1 s.

influence of an adjustable hydrostatic pressure difference. With this steady flow fluxes between 4 and 45 ml min^{-1} could be obtained. The suspension structure and particle motion were analysed from time resolved static light scattering. The optical cell was illuminated with a laser beam perpendicular to the flow direction. The scattering pattern was captured on a translucent screen and recorded on video. The recorded images arise from a superposition of scattering patterns from the complete cross section at mid-cell height. A typical rhcp light scattering pattern is shown in figure 2(a) for a deionized sample of PS120 at $n = 3\ \mu\mathrm{m}^{-3}$ and a flux of 8 ml min^{-1} (high scattering intensity is denoted by dark shading). The orientation of reflections with respect to the flow direction indicates that also in this shear geometry the hexagonal layers are oriented with the densest packed direction $\langle 111\rangle$ parallel to the flow direction. Note that here only a single hexagonal pattern is visible, indicating a cell filling sliding layer phase. In general, we identified rhcp and isotropic fluid phases as well as their coexistence. Additional microscopic inspection revealed that, as in the case of double wall restriction, the rhcp phase was always wall based. This non-equilibrium phase behaviour is similar to that observed in the cylindrical geometry of the 4 mm cross section, with the main difference being that there also an additional polycrystalline plug observable in the cell centre [48, 65].

Even with steady flow applied, the position of the Bragg maxima appeared to be moving under flow. We replaced the screen by a position dependent detector (SSO-DL100-7, Silicon Sensor GmbH, Berlin, Germany) positioned on the upper $\{10\}$ Bragg spot (chosen for its sensitivity to structural changes [36, 66]). The detector determines the motion of the centre of mass of the Bragg intensity distribution, which contains incoherently superimposed contributions from different cell depths. We observed centre of mass motions about the average position both in the radial and azimuthal directions $(\Delta r, \Delta\varphi)$ corresponding to compression/decompression in the flow direction, respectively, to rotation about the gradient direction. In figure 4(b) we give an example of a time trace recorded for the suspension of figure 4(a) over a time interval of 1 s. Amplitudes in the radial and azimuthal directions are about equal. Note the correlation between both motions on this timescale.

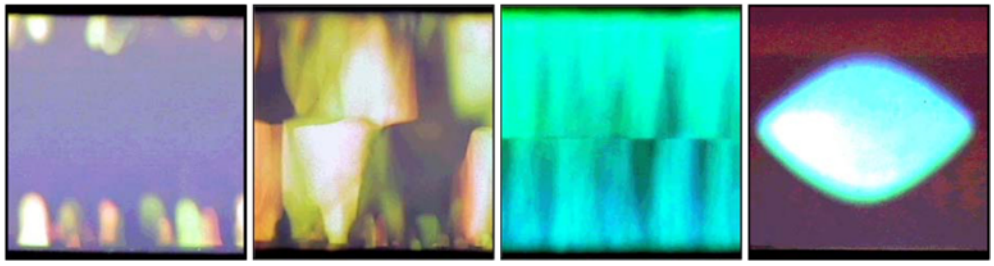

Figure 3. Images of colloidal crystals after complete solidification. Image height 2 mm. The interaction strength is increased from left to right by increasing n. One observes typical morphologies: caps, columns, wall crystal sheets, wall crystal (dark) plus bulk polycrystalline material. For details see text (images reproduced from [72]).

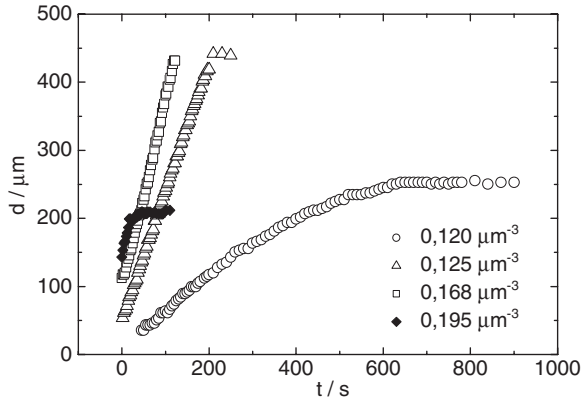

Figure 4. Growth curves for PS156 recorded at deionized conditions and at n values indicated. At coexistence ($n = 0.12\ \mu\mathrm{m}^{-3}$) growth is sublinear. Above melting ($n = 0.125$ and $0.168\ \mu\mathrm{m}^{-3}$) growth is linear and the growth velocity increases with n. Note the existence of a finite initial wall crystal thickness d_0 at zero time. At $n = 0.195\ \mu\mathrm{m}^{-3}$ growth is aborted by homogeneous nucleation.

The recorded time traces were Fourier analysed in both directions of reciprocal space (Ono-Sokki CF 300, NTD, JP) to obtain the power spectra of centre of mass motion. For interpretation the scattering volume is assumed to be composed of many subregions of different local shear rates and possibly different mechanisms of shear motion. Each scattering region contributes with its local vibration (rotational oscillation) frequency to the Δr ($\Delta\varphi$) spectrum. The spectral intensity $I(v)$ corresponds to the number of subregions vibrating with a given frequency and thus to the overall extension of regions shearing in a given mode. To be precise, we expect a zig-zag motion region to contribute to both Δr $\Delta\varphi$. In contrast no vibrations should be visible for the unregistered straight sliding mode.

2.4. Bragg microscopy for single wall confinement

During conditioning the suspension is continuously cycled through the tubing system and the cell. It is kept in a meta-stable non-equilibrium state but readily re-solidifies after cessation of shear. Bragg microscopy is a versatile tool to study colloidal crystals and their formation with a spatial resolution of some ten microns and a temporal resolution of video frequency [46, 67]. The method (and also polarization microscopy [68, 69]) has been used extensively before determining crystal growth velocities [7, 46] and homogeneous nucleation kinetics [70] to characterize sample morphologies [19, 71, 72], to study twinning patterns [67, 73, 74] or morphological changes under electrophoretic shear [75]. In this section we present a short description of the method, present the general scenario observed for charged sphere colloids and define the relevant quantities used for the systematic analysis used in the result section.

An optical flow through cell of rectangular cross section (2×10 mm^2) was mounted in side view (small side up) on the stage of an inverted microscope (Laborlux 12, Leitz, Wetzlar, Germany) equipped with a low resolution ($10\times$ or $20\times$) objective. The sample was illuminated from the side and crystals were observable if oriented properly to fulfil the Bragg condition. Typically a (110) reflection was chosen. Crystals of identical colour correspond to identical structure and orientation. Images are recorded by CCD-camera (EHD kamPro04, $1/2''$ SVHS, EHD Physikalische Technik, Damme, Germany) and stored in a computer for later image analysis.

Figure 3 shows a typical series as observed after re-solidification from PS120 shear melt. In side view the image height is 2 mm. The strength of interaction increases from left to right (here achieved by variation of n). Different solidification scenarios are observed. In fluid–bcc coexistence (left) cap like to tooth like crystals of random orientation are observed. These increase in volume as the interaction is increased. Above coexistence columns contact each other (middle left). A transition to a sheet like crystal morphology with preferred orientation (visible as single colour of the complete crystal) is observed slightly above melting (middle right). At still larger interaction homogeneous bulk nucleation occurs (right). Wall crystal growth is terminated by intersection with bulk crystals (here the illumination was altered to capture the Bragg reflection of the central bulk crystal). This series of transitions is typical for systems of bcc structure close to the fluid–bcc phase transition. It is observable both upon decreasing c at constant n and upon increasing n at constant c. It was also observed for PS156 and its mixtures with PS120, which are used below.

For some samples, however, we also observed a modification of the sheet morpohology. An example is shown in figure 8(b). In these we observed a non-Bragg-scattering region between the wall and the usual scattering region. The extension of this region is termed d^*. It was found to be constant in time.

We further measured the total crystal thickness $d(t)$ as a function of time. Examples are shown in figure 4 for deionized suspensions of pure PS156 at different n. $t = 0$ corresponds to stop of shear by an electromagnetic valve. The suspension comes to rest within less than 0.2 s. Also concerning the growth, different scenarios are observed corresponding to those discussed above. In coexistence growth is sub-linear. In all cases above coexistence linear growth is observed with the average growth velocity increasing with increased meta-stability. At elevated particle concentrations growth is aborted by intersection with homogeneously nucleated bulk crystals. Most important, above melting the extrapolation of data back to zero time yields a finite initial extension of the wall crystal $d(t = 0) \equiv d_0$. d_0 increases with increasing n. The same behaviour was observed for PS120 and its mixtures with PS156. Below we shall investigate in detail the dependence of d_0 and d^* on previous shear conditions and composition of the mixtures.

3. Results

3.1. Double wall restriction

For low shear rates the non-equilibrium phase diagram and the mode of motion of adjacent layers can be directly determined from video microscopy. In figure 5 we reproduce the low shear part of the non-equilibrium phase diagram for PS301 from [63]. Within the accessible range of shear rates all suspensions of bcc structure at rest showed rhcp structure under shear. Their solidification behaviour after cessation of shear was found independent of the modes of motion under shear (which have been discussed in detail in [64]). Registered sliding layer structures simply stay registered and the free sliding layers register within less than 0.2 s.

In both cases randomly stacked hexagonal close packed crystals are formed, which fill the complete cell (cf figure 1(d)). In a certain sense, at the shear rates accessible here, there is no classical heterogeneous nucleation event, because under shear, there exists no isotropic shear melt. This may well be the case at still larger shear rates, and experiments using a high speed camera are presently exploring this region.

The rhcp structure appears to be kinetically stabilized against relaxation to the equilibrium bcc structure. Transformation back to bcc occurs on the timescale of minutes to hours depending on the interaction parameters. It happens via nucleation with subsequent lateral growth. The actual nucleation mechanism is not yet clear. A snapshot of a just formed bcc region is shown in figure 6. Within the video time resolution available, the bcc region just appeared to be there from one frame to the next. Note that the crystal orientation is retained from the rhcp matrix and there seems to be some distortion of the matrix around this region.

Nucleation, however, is a rare event and we have only twice been able to directly observe the formation of a bcc region within the rhcp matrix. In most cases we were only able to observe the propagation of a bcc/rhcp phase or grain boundary through the imaged area at speeds of several microns per second. This way bcc crystals may grow very large (up to mm^2 area). They often appear to be twinned, similar to their macroscopic counter parts [67, 73].

3.2. Shear motion analysis in flow through cells

From the observations under shear in doubly restricted geometry one interesting question concerning the experiments in the flow through cell is, whether the registered zig-zag sliding to unregistered straight sliding transition also occurs in this geometry. To this end we first analysed the structural behaviour of PS120 under shear flow to identify a space filling rhcp structure. At low n and large c we observed near complete shear melting for all flow conditions. At larger n and deionized conditions we observed a sequence of different structures under flow. At very low fluxes polycrystalline plug-flow was observed, at very large fluxes near complete shear melting with narrow regions of a wall based layer structure was found ([53]; for a published example on a different system see [65]). At $n = 3\ \mu m^{-3}$ (corresponding to equilibrium bcc–fcc coexistence) a space filling rhcp structure was achieved over a wide range of fluxes (cf figure 2(a)).

For this suspension we first analysed the layer motion by recording the radial and azimuthal motion of the centre of mass of the $\{10\}$ Bragg reflection in reciprocal space. We observed some well reproducible qualitative features enabling us to discriminate three regimes of flow dynamics at fluxes of 4–13, 15–23 and 25–41 ml min^{-1}. At low fluxes we observed a strong coupling between the two directions of Bragg reflection motion indicating a coupling between a large amplitude periodic compression/decompression of layers in the flow direction (corresponding to Δr) and a large amplitude oscillation about the gradient direction (corresponding to $\Delta\varphi$) (cf figure 2(b)). At intermediate fluxes the coupling is weaker and the amplitude in both directions is reduced by about a factor of three. At large fluxes the amplitude in the azimuthal direction is again larger, while it stays small in the radial direction. The coupling is again clearly visible.

We then Fourier transformed the recorded time traces. Also here different features are observable for the three flux regions. For low to intermediate fluxes spectra of both directions are quite similar. Large flux spectra of the radial direction are similar to those recorded at intermediate fluxes. Large flux spectra of the azimuthal direction however differ from intermediate flux spectra. In figures 7(a)–(c) we therefore show the azimuthal motion spectra for the three regions.

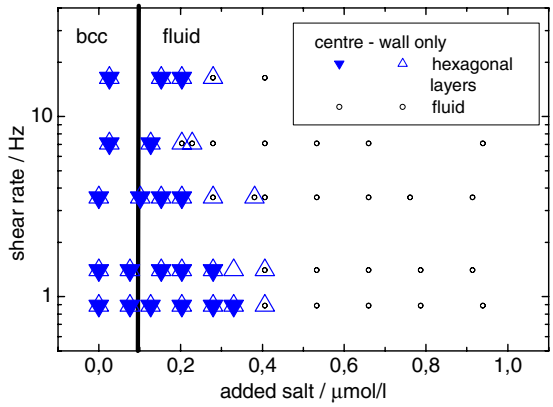

Figure 5. Non-equilibrium phase diagram for PS301 at $n = 0.15\ \mu\text{m}^{-3}$ under shear in the plate–plate shear cell (reproduced from [63]). Small circles denote fluid, triangles denote hexagonal layer structures. Up triangles were determined close to the cell wall, closed down triangles in the cell centre (15 μm off the wall). The vertical line marks the position of the bulk equilibrium phase bcc fluid boundary.

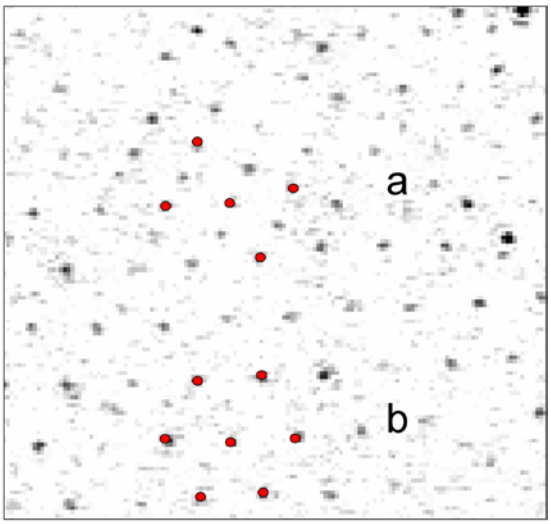

Figure 6. Example image of a nucleation event (at a) of the equilibrium bcc phase of PS301 within a rhcp matrix (b) close to the cell wall ($n = 0.15\ \mu\text{m}^{-3}$, $c = 1\ \mu\text{mol l}^{-1}$, $\dot{\gamma} = 4.5$ Hz). The image was taken some 20 min after cessation of shear. The imaged depth is about three layers with about 100 spheres in these having taken a bcc structure.

The most complex behaviour is observed at low fluxes of 4–13 ml min^{-1} (figure 7(a)). Here the total intensity first increases and the maximum frequency shifts from 25 to 45 Hz. This indicates that more and more regions are showing some oscillation about the gradient direction and that the maximum frequency of that oscillation increases. For fluxes above 8 ml min^{-1} the intensity of the low frequency part decreases, while the maximum frequency saturates. This indicates that fewer regions of low frequency oscillation are present and that oscillations disappear for frequencies larger than some critical frequency. Above 11 ml min^{-1} the high frequency intensity also decreases. At intermediate fluxes of 15–23 ml min^{-1} (figure 7(b)) the intensity shows a near exponential decrease with increasing frequency; it is independent of flux and small.

In general, the spectra are quite broad, as we detect signals from different cell depths (and thus shear regions) simultaneously. From hydrodynamics we take that the overall flow profile is parabolic, with possibly some minor modifications due to different viscosities for different

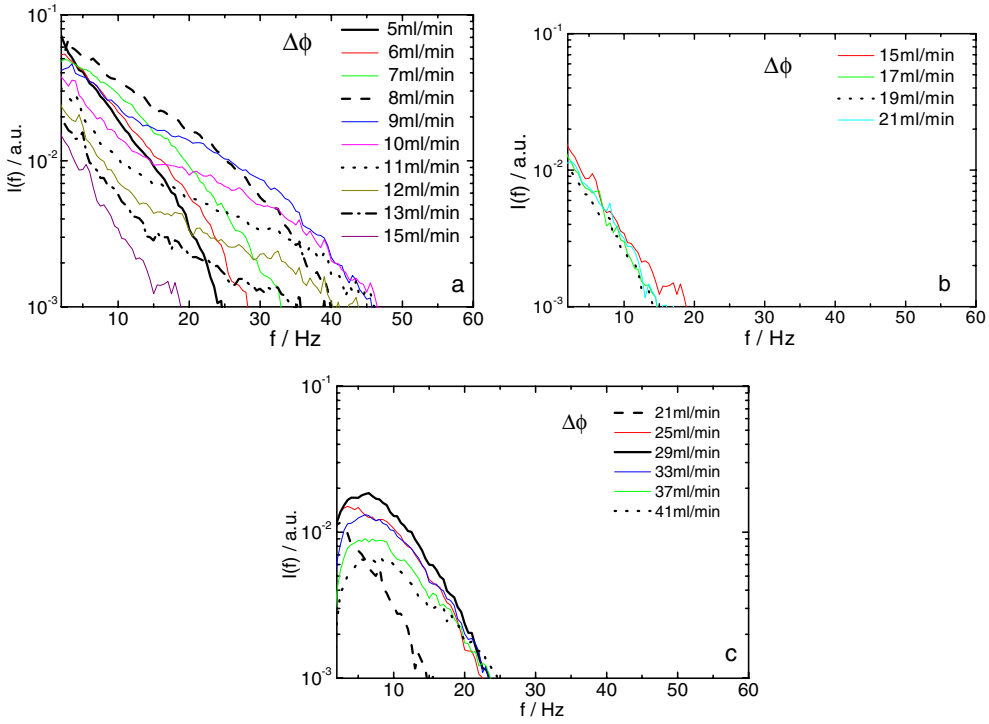

Figure 7. (a)–(c) Fourier transform spectra of the azimuthal motion of the upper {10} Bragg reflection of hexagonal layer phases of deionized PS120 at $n = 3\ \mu\mathrm{m}^{-3}$ under shear in a 1×10 mm flow through cell. The flow is driven by a hydrostatic pressure difference with parabolic flow profile. Total fluxes through the cell are indicated. Three distinct regions can be discriminated with increasing fluxes: (a) registered sliding with strong signal of the zig-zag motion of planes leading to a collective oscillation about the gradient direction. With increasing flux one observes first an acceleration of oscillations with a shift of the spectral signal towards larger frequencies followed by a transition to free sliding with a decay of the oscillating component, first at low then also at large frequencies. Note the comparably large width of the transition caused by the simultaneous presence of regions with different shear rates in the parabolic flow profile. (b) Free sliding motion with hardly any oscillatory signal. (c) Development and decay of an oscillation in plane resonance of freely sliding layers. The resonance frequency is at 7 Hz independent of the applied flux.

sliding mechanisms [65]. For increased flux the parabola will stretch. This will shift regions of constant shear rate inwards. We further assume that a registered sliding rhcp phase will show oscillations at a frequency of the zig-zagging, while a straight sliding phase will not. Then the observed behaviour at low fluxes can be interpreted as a general acceleration of oscillations within registered sliding rhcp regions with increased shear rates. The loss of low frequency intensity at larger fluxes is attributed to a disappearance of slow shearing regions of registered sliding layers. The existence of an upper frequency limit around 45 Hz is attributed to the disappearance of registered zig-zag sliding layers by transition to unregistered straight sliding. We therefore believe we are seeing the overall fingerprint of a registered to sliding transition occurring in the flux range of 9–13 ml min^{-1}, which starts at the cell walls and moves inward as the flux is increased.

At intermediate fluxes the complete system is in a straight sliding mode yielding only low spectral intensity. Finally, at higher fluxes between 25 and 37 ml min^{-1} the radial spectrum stayed at low intensities, while in the azimuthal spectrum we observed an additional in plane

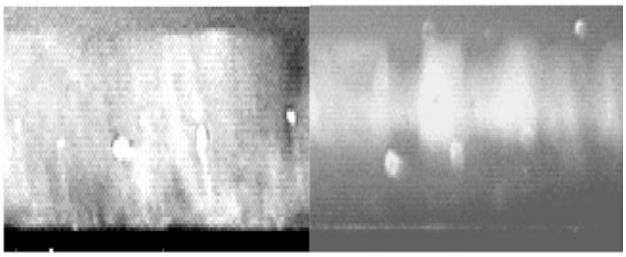

Figure 8. Bragg microscopic images of growing wall crystals of PS120 at $n = 0.67\ \mu\text{m}^{-3}$ and deionized conditions. Image height 320 μm. The left image was taken after slow shear, the right after fast shear. Images from different times were chosen to yield comparable total crystal thicknesses of $d \approx 260\ \mu$m. The crystal in the right image contains a non-scattering region of $d^* = 120\ \mu$m. d^* did not change in time.

oscillatory resonance located at $f = 7$ Hz, which had its maximum amplitude at 29 ml min^{-1} and is shown in figure 7(c). The origin of this resonance is not yet understood.

3.3. Solidification in the presence of a single wall

In nearly all cases of solidification from the shear induced sliding rhcp state we observed simple registering into a rhcp phase as initial step. The solidification process after cessation of shear is nevertheless not well understood in the above investigated region of the PS120 phase diagram where an equilibrium bcc–fcc coexistence occurs. Quite different morphologies are observed in the final state, including polycrystalline material with wall based rhcp layers, as yet unidentified distorted structures and coexistence of bcc and fcc single crystals (for an example of the latter prepared from shear melt rhcp coexistence under shear see [52]). We therefore continue with an exploration of the solidification scenario of PS120, PS156 and mixtures thereof in suspensions close to the fluid–bcc coexistence. There all samples solidify either from an isotropic shear melt or from a coexistence of wall based rhcp layers and shear melt.

Typical morphologies of wall based colloidal crystals grown from shear melts have been shown in figure 3. In our growth experiments on deionized PS120, PS156 and mixtures thereof, columnar growth was observed below n_F. Sheet like growth (cf figure 3(c)) was regularly observed for n somewhat larger than n_F, but still low enough to retain heterogeneous nucleation and subsequent growth, the dominant solidification mechanism. Two more examples of PS120 at $n \approx 0.67\ \mu\text{m}^{-3}$ are shown in figures 8(a) and (b). These were recorded during growth in the Bragg microscopic mode, with the illumination adjusted such that a bcc (110) reflection entered the microscope objective. Times were chosen to yield the same total crystal thickness $d(t)$. Figure 8(a) shows a homogeneous bcc sheet of $d(t) = 260\ \mu$m. The initial wall crystal thickness (from growth curves; see below) was $d_0 = 40\ \mu$m. This modification was observed most often at low n and low shear fluxes. In particular after shearing by large fluxes and/or larger n, we also observed a second modification shown in figure 8(b). A non-scattering (non-bcc) region of extension $d^* = 120\ \mu$m is observable between the wall and the scattering region. The total crystal extension again is $d(t) = 260\ \mu$m and the initial wall crystal thickness here was $d_0 = 130\ \mu$m. We explicitly note that in all our observations of a finite d^*, it was found to be constant in time. From a comparison to the registering processes observed in doubly restricted geometry and during solidification at larger n, we suspect an rhcp structure for the non-scattering region. However, an unequivocal proof by static light scattering remains to be performed. In any case the bcc crystal grows on top of some other structure serving as a

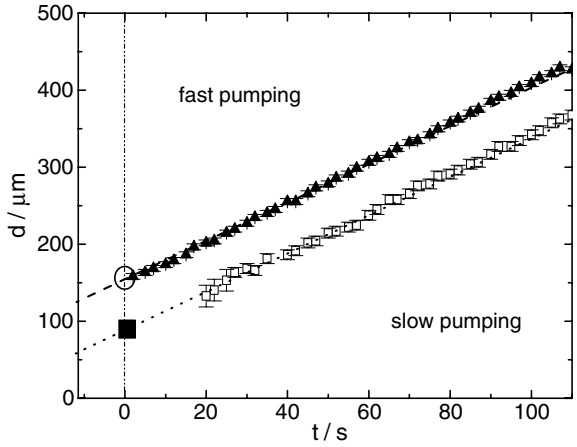

Figure 9. Extension d of wall crystals versus time for a mixture of PS156 and PS120 under deionized conditions, at $n = 0.47\ \mu\text{m}^{-3}$ and $p_{156} = n_{156}/n = 0.143$. The upper curve corresponds to an experiment after fast pumping yielding a growth velocity of $v = 2.60 \pm 0.01\ \mu\text{m s}^{-1}$ and an initial thickness $d_0 = 152\ \mu\text{m}$. The lower curve was recorded after slow pumping and yielded $v = 2.55 \pm 0.02\ \mu\text{m s}^{-1}$ and $d_0 = 83\ \mu\text{m}$. Lines are guides to the eye.

substrate. To support this idea of epitaxial growth on a precursor structure we next tried an estimate of the initial crystal size d_0 from quantitative growth measurements.

The growth curves of PS120, PS156 and their mixtures were measured by Bragg microscopy over a wide range of parameters. We here focus on the variations observed with a change of shear conditions and with system composition. Figure 9 shows two solidification runs performed under identical sample conditions but after shear melting with different pumping speed. While the growth velocity remained unaltered, the initial wall crystal extension d_0 was increased considerably in the case of fast pumping.

These experiments were repeated under variation of composition. We measured the initial wall crystal extension d_0 for PS120/PS156 at constant $n = 0.47\ \mu\text{m}^{-3}$ over a wide range of compositions expressed in terms of $p = n_{156}/n$. Irrespective of p this mixture solidifies in a random composition bcc structure. As PS156 is more highly charged, an increase of p at constant n corresponds to an increase of the pair interaction energy. Figure 10 shows that data taken after fast pumping lie systematically above those taken after slow pumping. For both fast and slow pumping speeds d_0 increases nearly linearly with increasing p. To relate these findings to the phase behaviour, we adapt a suggestion by Aastuen *et al* from their pioneering work on bulk crystal growth [74]. We express the meta-stability of our sample in terms of $n - n_{\text{F}}(p)$, where we assume that the phase diagram as a function of n and p shows a straight line connecting the known n_{F120} with n_{F156}. As $n > n_{\text{F}}(p)$ for all samples and further $n_{F120} > n_{F156}$ the increase in p also correspond to an increase of metastability of the melt [7, 46, 74]. In figure 11 we re-plot d_0 versus $n - n_{\text{F}}(p)$. The data for both shear conditions arrange on straight lines. The initial wall crystal thickness increases with increased melt meta-stability. For both data sets an extrapolation to the point of disappearance of d_0 yielded $n - n_{\text{F}}(p) \approx 0.05$. Thus d_0 disappears considerably above freezing. From measurements of the final extension of the observed wall crystals we further know that in all cases of finite d_0 we obtain cell filling crystals, i.e. n is also above n_{M}. Similar data were taken on a slightly different sample of 100 nm diameter. Also these yielded a point of disappearance clearly above n_{F} and close to n_{M}. We explicitly note that from the microscopic observations

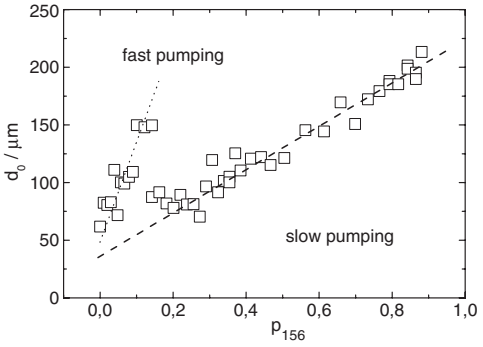

Figure 10. Initial wall crystal extension d_0 for PS120/PS156 measured for two different pumping speeds versus composition $p_{156} = n_{156}/n$. Data taken after fast pumping lie systematically above those taken after slow pumping. Both data sets show a linear relation with n. Lines are guides to the eye.

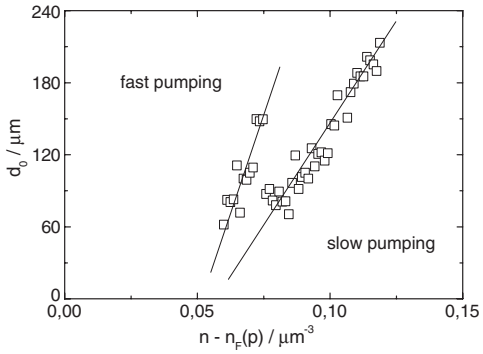

Figure 11. Initial wall crystal extension d_0 for PS120/PS156 measured for different p and two different pumping speeds versus distance from the freezing transition $n - n_F(p)$. Both data sets show a linear relationship and extrapolate to zero for similar finite $n - n_F(p)$. Lines are guides to the eye.

of the morphology we find that this point of vanishing d_0 closely correlates with the observed transition between random orientation columnar growth and oriented sheet growth [72].

4. Discussion

4.1. Structure and motion under shear

We now may compare our two sets of experiments performed in a doubly restricted geometry under linear shear and in single wall confinement with position dependent shear rates. In both cases we observed the existence of hexagonal close packed layers parallel to the cell walls and with the densest packed direction in-plane oriented parallel to the shear direction. In both cases such registered or free sliding layer phases may fill the complete cell, given the equilibrium structure is crystalline. The transition from registered to free sliding was found to be triggered by increased shear rates. In the doubly restricted geometry we were able to directly observe the scenario, while in the other case we found evidence for its occurrence from Bragg spectroscopy.

Both series of experiments thus were observed to yield strikingly similar scenarios under shear. A possible difference could be the extension of wall based layer structures under shear. In the present experiments we could only give an estimate for the single wall case. In future experiments we shall also vary the gap width of our plate–plate shear cell. Then also there the extension of wall based layer structures shall be determined quantitatively.

We also did not observe other influences of confinement. Examples of additional effects for systems at rest are already found in the literature. Hug and van Swol studied slits confined near hard sphere particles at elevated c and slit widths below ten layers [76]. Messina and Löwen simulated the phase behaviour of two layer systems with a large variation of interaction range [42]. Both cases suggest that the compatibility between gap thickness and interlayer spacing is a necessary ingredient for long range order. An example of compatibility effects under shear was observed on the molecular scale by Gee *et al* [77]. In their surface force apparatus experiment on cyclohexane, the gap width was observed to be self-adjusting to always allow for layered flow. We expect similar effects to appear also for colloidal systems and first steps in that direction have recently been reported for hard sphere systems [78]. The

absence of such effects in the present case may partly be due to the fact that 15 layers are still relatively close to the bulk situation. On the other hand, in our long range interactions, mobile particles are still in contact with an (unsheared) reservoir of macroscopic dimensions. They may therefore 'escape' from the slit geometry to allow for an integral layer number. This may go unnoticed as the corresponding changes of n in the slit region are small and fall below our uncertainty of direct density measurements. Changes of n in the reservoir are even smaller.

4.2. Competing kinetic processes after cessation of shear

Immediately after cessation of shear different processes may occur. We have observed simple registering of sliding layers in both the plate–plate shear cell and the flow through geometry at large n. From the observation of a finite initial wall crystal thickness d_0 and the existence of non-bcc-scattering regions of similar thickness in the final crystal, we presume that registering also happens in single wall confinement at low n. There, however, the layer structures under shear do not fill the complete cell, which restricts the extension of any registered structures after cessation of shear. d_0 shows an increase with increasing interaction strength, respectively, melt metastability. This compares well with the observed phase behaviour under shear, where the layer phase became more stable with increased n. It is therefore tempting to identify the initial wall crystal thickness with the extension of shear induced layers. The bcc phase may then grow on top of the freshly registered rhcp solid. In fact, returning to figure 8(b) the extension of the non-scattering region was found to be $d^* = 120$ nm, while the corresponding growth curves yielded $d_0 = 130$ nm. A similar agreement between d_0 and d^* was observed for most cases of large $d^* > 100$ μm.

There are, however, three subtle problems with this simple picture which need further attention. First, the sheet morphology shows large scale and near complete orientation of $\langle 111 \rangle$ in the direction of formerly applied shear. Here layer phases survived to form an oriented nucleus. On the other hand, at coexistence and slightly above, suspensions solidify in a cap like or columnar morphology with the $\{110\}$ plane parallel to the wall, but a more or less random orientation of the closest packed direction therein. Therefore any shear induced layer phase must have dismantled before the nucleation of individual columns. Consequently we have to anticipate some (possibly diffusive?) disintegration of the meta-stable layers in contact with the shear melt which will compete with the nucleation of the stable bcc phase. Therefore, one may not expect exact quantitative agreement between d_0 and the original layer phase extension. Rather d_0 only gives a lower boundary for the shear layer extension.

Second, the investigations in the doubly restricted geometry have shown that in the case of coexistence between layer phases and fluid, the former are always wall based. Upon decreasing c their extension increased successively until they became space filling. In the flow through cell the stability of the layer phase could be increased by increasing n. Both observations correlate with the increased extension of the initial wall crystal d_0 upon increasing the interaction strength by increasing n. On the other hand, d_0 was observed to *increase* with increased shear, while according to the structure analysis in both geometries the stability of the bulk layer phase *decreased* with increased flux. This seemingly creates a contradiction. However, previous investigations indicated that a residual wall based layer structure can be present even in very large fluxes, where the bulk suspension is already of fluid structure [48, 65]. Moreover, experiments and simulations show both shear induced melting and ordering with significant differences in the phase behaviour with and without walls present [36, 79, 80]. Therefore we should not expect a trivial correlation between d_0 and the stability of the bulk layer phase. Rather we suggest directly measuring the extension of wall based layers under shear (e.g. by Bragg microscopy [48] or in the doubly restricted geometry at large plate separations).

Finally, d_0 was observed to nearly coincide with d^* for large d_0. This of course supports the above picture of a registered layer phase acting as structured substrate for the nucleation and subsequent growth of bcc crystals. However, this cannot be the whole story, as for small d_0 the final crystal was of bcc structure only. In fact, for figure 8(a) $d^* = 0$, while from the growth measurements $d_0 = 40\ \mu$m. Such an absence of a non-scattering region was also regularly observed, albeit only for small $d_0 < 70$–$80\ \mu$m. Any registering therefore must be followed by a symmetry breaking structural transformation to the equilibrium phase. At present it is not clear what the nature of the rhcp–bcc transformation is (is it martensitic, like observed before in confined suspensions [50]?), what the relevant timescales are (does it happen before, after or upon coverage of the rhcp phase with bcc?) or how it relates to the twinning patterns observed [67]. A considerably improved temporal resolution of the experiments is needed to answer these points.

5. Conclusions

We have conducted a series of experiments addressing the issue of heterogeneous nucleation under the combined influence of shearing fields and confining geometry. We conclude with the preliminary picture of the scenario evolving for this particular study. We observed that both in a single wall and a double wall confinement shear will lead to the formation of layer structures (be it a bulk stable phase or a layering mediated local effect). Upon cessation of shear, large scale single crystallites of preferred orientation occur through registering of the layers, if the previous layer structures were space filling. The mode of motion under shear was observed to be of no significant influence on the resulting solids after shear. In doubly restricted geometry nucleation of bcc from such a meta-stable rhcp matrix is a rare event. Nevertheless, large scale single (sometimes twinned) crystallites evolve through lateral growth.

Under single wall restriction with non-space filling layer structures under shear the scenario was observed to be more complex. We presume that in a first step here the sliding layer phase precursors also register to form a rhcp structure. Here, however, the (kinetically?) stabilizing influence of the second wall is missing and below a certain value of meta-stability of the melt these initial oriented structures will disappear and be replaced by individually nucleated crystals of random orientation. In coexistence the latter grow to cap-like, pillar-like or columnar structures. Above coexistence columns were observed to meet and fill the complete cell. The situation changes as a certain value of meta-stability is exceeded: above a certain value of $n > n_M$ we observe growth of large single crystals of a preferred orientation retained from the sheared state. If the initial rhcp precursors are of large vertical extension, (at least) part of them is be covered by bcc growing on top. Else they transform to bcc by a mechanism still unknown.

We believe that all these phenomena are due to competition between two kinetic mechanisms, one trying to dissolve the meta-stable precursors by diffusion and one assembling the melt into bcc nuclei. The latter one may be substantially assisted by the presence of the remaining precursors, providing a flat, pre-structured substrate.

We hope to have contributed some fascinating observations on different heterogeneous nucleation processes after shear and their consequences for crystal growth. We further hope to have stirred up interest in the theory and simulation to provide insights from different systems and possibly also from different points of view. The final goal set is both a more detailed understanding and more general conceptualization of these important non-equilibrium processes.

Acknowledgments

It is a pleasure to acknowledge intense discussions with A v Blaaderen, A Imhoff, M Leunissen and P Royal on technical points and the differences between charged and hard sphere systems

under shear. For stimulating discussions on the influence of confining geometries we are grateful to H Löwen and R Messina and on shear in general to J K G Dhont. This work was financially supported by the DFG (Grants SFB TR6 TPD1, Pa 459/8 and Pa459/12), the MCRT Network 'Dynamic Arrest' (MRTN-CT-2003-504712), Stiftung Rheinland Pfalz f. Innovation (386261/588) and the MWFZ Mainz. This is gratefully acknowledged.

References

[1] Asher S A, Weissmann J, Sunkara H B, Pan G, Hotz J, Liu L and Keesavamoorthy R 1997 *Photonic and Optoelectronic Polymers* (*ACS Symp. Series* vol 672) (Washington, DC: American Chemical Society) pp 495–506
[2] Crocker J C and Grier D G 1998 *Mater. Res. Soc. Bull.* **23** 24
Murray C 1998 *Mater. Res. Soc. Bull.* **23** 33
van Blaaderen A 1998 *Mater. Res. Soc. Bull.* **23** 39
Asher S A, Holtz J, Weismann J and Pan G 1998 *Mater. Res. Soc. Bull.* **23** 44
[3] Luck W, Klier M and Wesslau H 1963 *Ber. Bunsenges Phys. Chem.* **67** 75
Luck W, Klier M and Wesslau H 1963 *Ber. Bunsenges Phys. Chem.* **67** 84
Luck W, Klier M and Wesslau H 1963 *Naturwissenschaften* **50** 485
[4] Robbins M O, Kremer K and Grest G S 1988 *J. Chem. Phys.* **88** 3286
[5] Hynninen A and Dijkstra M 2002 *Phys. Rev.* E **68** 021407
[6] Yethiraj A and Blaaderen A v 2003 *Nature* **421** 513
[7] Palberg T 1999 *J. Phys.: Condens. Matter* **11** R323–60
[8] Stipp A, Heymann A, Sinn Chr and Palberg T 2001 *Prog. Colloid Polym. Sci.* **118** 266
[9] Dixit N M and Zukoski C F 2001 *Phys. Rev.* E **66** 051602
[10] Anderson V J and Lekkerkerker H N W 2002 *Nature* **416** 811
[11] Zhou B, Hu Z and Wu J B 2003 *Phys. Rev. Lett.* **90** 049304
[12] Harland J L and van Megen W 1996 *Phys. Rev.* E **55** 3054–67
[13] Wette P, Schöpe H J, Liu J and Palberg T 2003 *Europhys. Lett.* **64** 124–30
[14] Auer S and Frenkel D 2001 *Nature* **409** 1020
Auer S and Frenkel D 2002 *J. Phys.: Condens. Matter* **14** 7667
[15] O'Malley B and Snook I 2003 *Phys. Rev. Lett.* **90** 085702
[16] Auer S and Frenkel D 2001 *Nature* **413** 711
[17] Bartlett P and Megen W v 1994 *Granular Matter* ed A Mehta (New York: Springer) pp 195–257
[18] Schilling T and Frenkel D 2004 *Phys. Rev. Lett.* **92** 085505
[19] Gast A P and Monovoukas Y 1991 *Nature* **351** 552
[20] He Y, Olivier B and Ackerson B J 1997 *Langmuir* **13** 1408–12
[21] Russel W B, Chaikin P M, Zhu J, Meyer W V and Rogers R 1997 *Langmuir* **13** 3871
[22] Henderson S I, Mortensen T C, Underwood S M and van Megen W 1996 *Physica* A **233** 102
[23] van Megen W 2002 *J. Phys.: Condens. Matter* **14** 7699–717
[24] Sullivan M, Zhao K, Harrison Chr, Austin R H, Megens M, Hollingsworth A, Russel W B, Cheng Z, Mason T and Chaikin P M 2003 *J. Phys.: Condens. Matter* **15** 11
[25] Yamanaka J, Murai N, Iwayama Y, Yonese M, Ito K and Sawada T 2004 *J. Am. Chem. Soc.* **126** 7156
[26] Ackerson B J, Paulin S E, Johnson B, van Megen W and Underwood S 1999 *Phys. Rev.* E **59** 6903
[27] Hoogenboom J P, van Langen-Suurling A K, Romijn J and van Blaaderen A 2004 *Phys. Rev.* E **69** 051602
[28] Ristenpart W D, Aksay I A and Saville D A 2003 *Phys. Rev. Lett.* **90** 128303
[29] Holgado M *et al* 1999 *Langmuir* **15** 4701–4
[30] Schöpe H J 2003 *J. Phys.: Condens. Matter* **15** L533–40
[31] Tang Y, Malzbender R M, Mockler R C and O'Sullivan W J 1987 *J. Phys. A: Math. Gen.* **20** L189–92
[32] Yin Y, Li Z-Y and Xia Y 2003 *Langmuir* **19** 622
[33] Lin K-h, Crocker J C, Prasad V, Schofield A, Weitz D A, Lubensky T C and Yodh A G 2000 *Phys. Rev. Lett.* **85** 1770–3
[34] Palberg T, Mönch W, Schwarz J and Leiderer P 1995 *J. Chem. Phys.* **102** 5082–7
[35] Okubo T and Ishiki H 1999 *J. Colloid Interface Sci.* **211** 151
[36] Ackerson B J 1983 *Physica* A **128** 221
[37] Haw M D, Poon W C K and Pusey P N 1998 *Phys. Rev.* E **57** 6859
Haw M D, Poon W C K and Pusey P N 1998 *Phys. Rev.* E **58** 4673
[38] Blaak R, Auer S, Frenkel D and Löwen H 2004 *J. Phys.: Condens. Matter* **16** S3873

[39] van Winkle D H and Murray C A 1986 *Phys. Rev.* A **34** 562
[40] Schmidt M and Löwen H 1996 *Phys. Rev. Lett.* **76** 4552–5
[41] Neser S, Bechinger C, Leiderer P and Palberg T 1997 *Phys. Rev. Lett.* **79** 2348
[42] Messina R and Löwen H 2003 *Phys. Rev. Lett.* **91** 146101
[43] Auer S and Frenkel D 2003 *Phys. Rev. Lett.* **91** 015703
[44] Dozier W D and Chaikin P M 1982 *J. Physique* **43** 843
[45] Stevens M J and Robbins M O 1993 *Phys. Rev.* E **48** 3778
[46] Würth M, Schwarz J, Culis F, Leiderer P and Palberg T 1995 *Phys. Rev.* E **52** 6415–23
[47] Rastogi S R, Wagner N J and Lustig S R 1996 *J. Chem. Phys.* **104** 9234
Rastogi S R, Wagner N J and Lustig S R 1996 *J. Chem. Phys.* **104** 9249
[48] Hünerbein S v, Würth M and Palberg T 1996 *Prog. Colloid Polym. Sci.* **100** 241
[49] Löwen H 2001 *J. Phys.: Condens. Matter* **13** R415–32
[50] Heymann A, Stipp A, Sinn Chr and Palberg T 1998 *J. Colloid Interface Sci.* **207** 119–27
[51] Weiss J A, Oxtoby D W, Grier D A and Murray C A 1995 *J. Chem. Phys.* **103** 1180
[52] Schöpe H-J, Decker Th and Palberg T 1998 *J. Chem. Phys.* **109** 10068
[53] Preis Th 2004 *PhD Thesis* Mainz
Preis Th, Biehl R and Palberg T, unpublished
[54] Palberg T, Härtl W, Wittig U, Versmold H, Würth M and Simnacher E 1992 *J. Phys. Chem.* **96** 8180
[55] Evers M, Garbow N, Hessinger D and Palberg T 1998 *Phys. Rev.* E **57** 6774
[56] Liu J, Schöpe H J and Palberg T 2000 *Part. Part. Syst. Charact.* **17** 206–12
Liu J, Schöpe H J and Palberg T 2000 *Part. Part. Syst. Charact.* **18** 50 (erratum)
[57] Wette P, Schöpe H-J, Biehl R and Palberg T 2001 *J. Chem. Phys.* **114** 7556
[58] Lide D R (ed) 1992 *Handbook of Chemistry and Physics* 73rd edn (Boca Raton, FL: CRC Press)
[59] Liu J, Stipp A and Palberg T 2001 *Prog. Colloid Polym. Sci.* **118** 91
[60] Palberg T, Medebach M, Garbow N, Evers M, Barreira Fontecha A, Reiber H and Bartsch E 2004 Electrophoresis of model colloidal spheres in low salt aqueous suspensions *J. Phys.: Condens. Matter* **16** S4039
[61] Wette P, Schöpe H J and Palberg T 2002 *J. Chem. Phys.* **116** 10981
[62] Biehl R and Palberg T 2004 *Rev. Sci. Instrum.* **75** 906
[63] Biehl R and Palberg T 2003 *Proc. R. Chem. Soc. Faraday Discuss.* **123** 133
[64] Biehl R and Palberg T 2004 Modes of motion in sheared colloidal suspensions *Europhys. Lett.* **66** 291
[65] Preis T, Biehl R and Palberg T 1998 *Prog. Colloid Polym. Sci.* **108** 129–33
[66] Loose W and Ackerson B J 1994 *J. Chem. Phys.* **101** 7211
[67] Maaroufi M R, Stipp A, Preis T and Palberg T 2001 *Sci. Tech. Information* **CDR 5** 35
[68] Monovoukas Y, Fuller G G and Gast A P 1993 *J. Chem. Phys.* **93** 8294
[69] Pan G, Sood A K and Asher S A 1998 *J. Appl. Phys.* **84** 83
[70] Aastuen D J W, Clark N A, Swindal J A and Muzny C D 1990 *Phase Transitions* **21** (2–4) 139
Maaroufi M R, Stipp A, Preis T and Palberg T 2001 *Sci. Tech. Information* **CDR 5** 35
[71] Okubo T 1994 *Macro-ion Characterization: From Dilute Solution to Complex Fluids* (*ACS Symp. Series* vol 548) ed K S Schmitz (Washington, DC: American Chemical Society) p 364
[72] Liu J, Schöpe H J and Palberg T 2001 *J. Chem. Phys.* **116** 5901
[73] Liu J and Palberg T 2004 *Prog. Colloid Polym. Sci.* **123** 222
[74] Aastuen D J W, Clark N A, Kotter L K and Ackerson B J 1986 *Phys. Rev. Lett.* **57** 1733
Aastuen D J W, Clark N A, Kotter L K and Ackerson B J 1986 *Phys. Rev. Lett.* **57** 2772 (erratum)
[75] Medebach M and Palberg T 2004 *Prog. Colloid Polym. Sci.* **123** 260
[76] Hug J E, van Swol F and Zukoski F 1995 *Langmuir* **11** 111–8
[77] Gee M L, McGuiggan P M, Israelachvili J N and Homola A M 1990 *J. Phys. Chem.* **93** 1895
[78] Derks D, Wisman H, van Blaaderen A and Imhof A 2004 *J. Phys.: Condens. Matter* **16** S3917
[79] Stevens M J and Robbins M O 1993 *Phys. Rev.* E **48** 3778
[80] Rastogi S R, Wagner N J and Lustig S R 1996 *J. Chem. Phys.* **104** 9234
Rastogi S R, Wagner N J and Lustig S R 1996 *J. Chem. Phys.* **104** 9249